Considerations in phase plane analysis for nonstationary reentrant cardiac behavior

Mark-Anthony Bray[1,*] and John P. Wikswo[2]
[1]*Department of Biomedical Engineering, Vanderbilt University, Nashville, Tennessee 37235*
[2]*Department of Physics and Astronomy, Vanderbilt University, Nashville, Tennessee 37235*
(Received 9 May 2001; revised manuscript received 17 August 2001; published 2 May 2002)

Cardiac reentrant arrhythmias may be examined by using time-series analysis, where a state variable is plotted against the same variable with an embedded time delay τ to form a phase portrait. The success of this procedure is contingent upon the resultant phase-space trajectories encircling a fixed origin. However, errors in interpreting the dynamics of phase singularities associated with reentry may arise due to the trajectories not encircling the origin or due to a poor choice of τ. We demonstrate an algorithm which is capable of establishing proper orbits without the need to specify τ. We find that phase singularities could be localized closer to the point of initial formation than was possible previously, which is important for the purposes of singularity tracking and investigating electrodynamic interactions.

DOI: 10.1103/PhysRevE.65.051902 PACS number(s): 87.10.+e, 82.40.Ck, 05.45.Tp, 87.19.Hh

I. INTRODUCTION

Phase plane analysis has recently offered a unique perspective into cardiac fibrillatory behavior [1–4]. An excitable element may be mapped into phase space by plotting a state variable against another variable; for example, the two-variable FitzHugh-Nagumo model allows for phase space to be examined in terms of excitability versus refractoriness [5]. Normally, an excitable element remains at one stable location in phase space until a superthreshold stimulus perturbs the system and forces the element into a closed-loop trajectory about an attractor.

For practical purposes, an experimenter may not have direct access to multiple, concurrent state variables in order to perform a dynamical systems analysis. However, using time-series analysis, a topologically equivalent attractor may be reconstructed given only one component of the system [6,7]. For N evenly sampled values of $y(t)$, the attractor in two dimensions is $y_i=(y(i),y(i+\tau))$ where τ is the time-embedding lag and $i=1,\ldots,N\text{-}1$.

Given a spatiotemporal activation sequence, we can use time-series analysis to reconstruct a phase-space trajectory by using the transmembrane potential $V(t)$ as a state variable, and plotting it against $V(t+\tau)$. Typically, τ is usually calculated as the first zero crossing of the autocorrelation function for the data in order to insure linear independence between the two state variables [8]. We may then define phase θ as the angle made by the phase-space trajectory with respect to a central origin at a particular instant in time [1].

Rotors are regions of excitability rotating around a central spatial location. In phase space, this point corresponds to the phase singularity, a topological defect where all phase values (i.e., $-\pi$ to π) converge and the phase itself at that point is undefined [9]. An example is shown in Fig. 1(a); here, an isochronal activation map is used to highlight the location of the rotor and the motion of the wave around it. Regions around the phase singularity are characterized by low-amplitude oscillations [10,11]. In the phase plane, these correspond to rotations with a small circumferential length.

As described by Gray *et al.*, [1] a fixed origin in the phase plane is defined by using the average value V_{mean} of the state variable $V(t)$ for the entire sequence about which the instantaneous phase angle is determined. However, in the case of unstable or drifting reentrant patterns such as fibrillation, low-amplitude passive responses may occur as the vortex meanders through or near a particular location. Therefore, one limitation of this approach is that, for such a site, all cycles in the phase plane may not encircle the origin as defined by V_{mean}, as shown in Fig. 1(c). In addition, the selection of embedding delay τ is critical; a nonoptimal choice of τ may lead to a low-quality reconstruction of phase space. If τ is too small, then $V(t)\approx V(t+\tau)$ (i.e., the values are highly correlated), resulting in the trajectories being concentrated on the diagonal in the reconstructed phase space, as shown in Fig. 2(a). An overly large choice of τ leads to decorrelation of the data, resulting in stretching and deformation of the phase trajectories as the structure of the attractor is destroyed. If we define a proper rotation as one which has a definite direction and a unique center of rotation, we see from Fig. 2(b), this choice of τ leads to several improper rotations along the trajectory, which will yield a distorted calculation of phase about V_{mean}. This in turn could lead to errors in interpreting the dynamics of phase singularities associated with reentry. Furthermore, during full fibrillation, the number of wave fronts and wave morphology changes unpredictably. Hence, the optimal value of τ as calculated by the autocorrelation method may not be unique for the entire spatiotemporal course of recorded activity. We propose an alternate method of reconstructing the phase space which takes into account the nonstationary nature of fibrillatory behavior and the pitfalls of a nonoptimal choice of τ.

*Author to whom correspondence should be addressed. Present address: Department of Biomedical Engineering, Vanderbilt University, 5824 Stevenson Center, Nashville, TN 37232; Electronic address: mark.bray@vanderbilt.edu

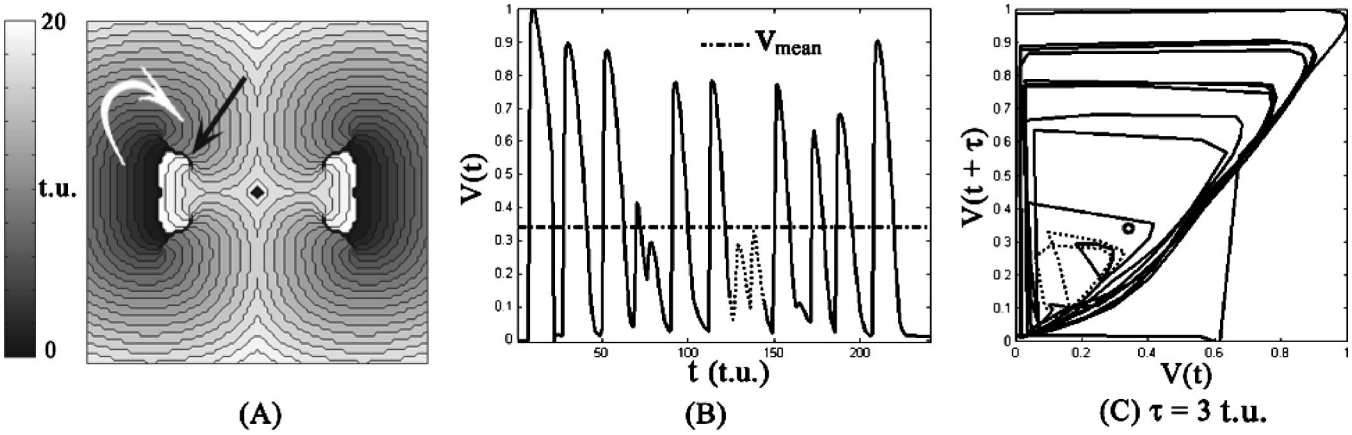

FIG. 1. (a) An isochronal map from numerically simulated data. The white arrow indicates the direction of wave rotation. (b) Transmembrane signal measured at the site indicated by the black arrow in (a). Oscillations falling below the mean value, V_{mean}, of the signal are shown with dotted lines. (c) Phase portrait of the signal shown in (b) using $\tau=3$. The origin (V_{mean}, V_{mean}) is indicated by a circle.

II. METHODS

The primary difficulty in calculating phase for this variety of oscillatory behavior is the presence of multiple centers of rotation in the phase plane during the temporal evolution of the system. A solution is to modify the state variable in an attempt to insure a fixed center of rotation [12]. This procedure is dependent on the proper implementation of the empirical mode decomposition (EMD) [13], which divides the signal into a series of intrinsic mode functions, each of which represents an oscillation frequency embedded within the signal. However, the process grants proper rotations to *all* deflections in the signal, regardless of amplitude. Therefore, oscillations stemming from noise are treated the same as oscillations generated from action potential propagation. A companion problem is the iterative nature of the procedure, which can result in inappropriate exaggeration of even the most minute deflections. Therefore, there is not necessarily a good correlation between an intrinsic mode of a temporal signal at a particular location and its neighbor. Hence, the EMD does not easily lend itself to analysis of a spatially distributed series. We have modified the algorithm in order to include considerations unique to cardiac data.

A. The pseudo-EMD (PEMD)

Since not every oscillation in the data is significant, the first task is to determine which oscillations are given proper rotations in the phase plane. To this end, the algorithm first performs a PEMD upon the data. First, we construct two envelope curves which connect the maxima $V_{max}(t)$, and minima $V_{min}(t)$, of the wave form. This is performed by applying a sliding maximum and minimum filter to the data. The length of the filter window is determined in the following way. The period of the reentrant activity was estimated on the basis of the dominant frequency component of the data; since much of tissue is at some distance from the phase singularities present, it was assumed that the period obtained would be representative of single-action potentials alone. Since reentry may be characterized by double-humped potentials [14,15], we then used half this value as the filter window length in order to also isolate the double peaks. Applying these two filters and subtracting the results will yield zeros surrounding the extrema. The result can further be processed to produce the actual extrema points. As opposed to [13], we have chosen to use piecewise cubic Hermite rather than cubic spline interpolation to connect the extrema since cubic spline interpolation may create large swings between

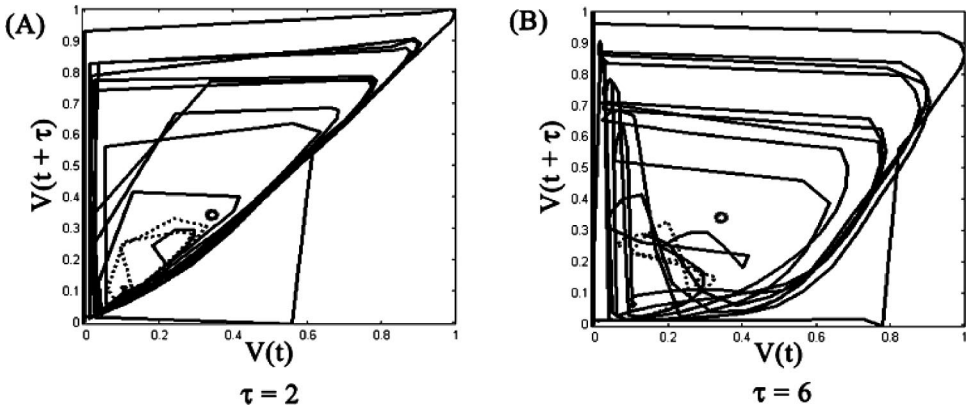

FIG. 2. Example of phase-space trajectories resulting from poor choices of τ. (a) $\tau=3$. (b) $\tau=6$.

extrema. The envelope midline $V^*_{mean}(t)$ is then computed as $[V_{max}(t)+V_{min}(t)]/2$. We then detrend $V(t)$ by computing $V'(t)=V(t)-V^*_{mean}(t)$. In this way, we create a rough approximation of an intrinsic mode function with the pertinent frequency information desired.

B. The Hilbert transform

Mathematically, a function and its Hilbert transform are orthogonal over the infinite interval. Hence plotting $V'(t)$ against its Hilbert transform will yield proper rotations in the phase plane. The Hilbert transform is calculated as [16]

$$H[V'(t)]=\frac{1}{\pi}\mathrm{P}\left[\int_{-\infty}^{\infty}\frac{V'(T)}{t-T}dT\right], \tag{1}$$

where P is the Cauchy principal value of the integral. For practical purposes, this integral is never actually calculated; it is obtained from $V'(t)$ by a filter with a unity amplitude response and a phase response with a constant $\pi/2$ lag at all frequencies. $V'(t)$ and $H[V'(t)]$ may be combined as complex conjugates to form an analytical signal,

$$\tilde{V}(t)=V'(t)+JH[V'(t)]=A(t)e^{i\theta(t)}, \tag{2}$$

where $A(t)$ is an amplitude function, and $\theta(t)$ is a phase function.

The application of the PEMD and the Hilbert transform is displayed in Fig. 3 for a numerically simulated signal.

C. Calculation of phase

Using a constant V_{mean}, the spatial phase map for each coordinate (x,y) is calculated as

$$\theta(x,y,t)=\arctan\left[\frac{V(x,y,t+\tau)-V_{mean}(x,y)}{V(x,y,t)-V_{mean}(x,y)}\right], \tag{3}$$

whereas the expression of phase using the Hilbert transform is

$$\theta(x,y,t)=\arctan\left[\frac{V'(x,y,t)}{H[V'(x,y,t)]}\right]. \tag{4}$$

The formulation of θ in Eq. (4) is the same as what follows from the definition of the analytical signal given in Eq. (2). Also note that the formulation is independent of any time-embedded delay τ.

D. Numerical Simulation and Experimental Preparation

The numerical methods are identical to those described previously [11,17]. The tissue was modeled as a three-dimensional (3D) bidomain using the Beeler-Reuter model for the active membrane kinetics

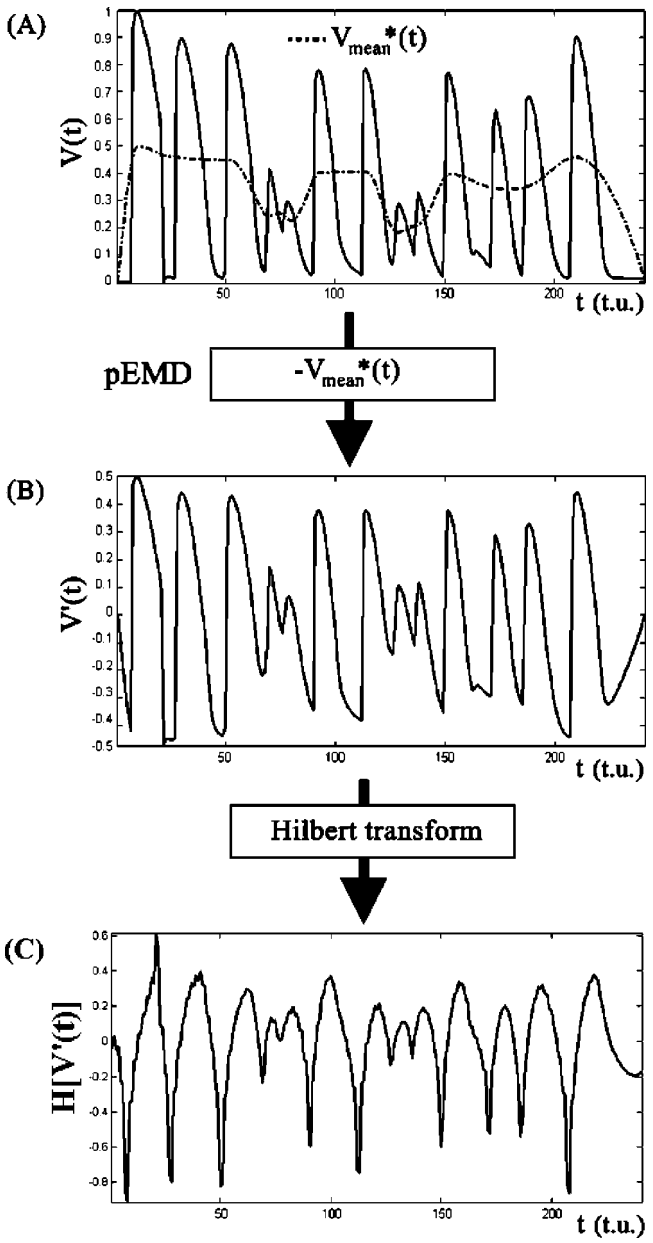

FIG. 3. Flowchart of the algorithm as applied to numerically simulated data. (a) $V(t)$ with $V^*_{mean}(t)$ shown as a broken line. (b) $V'(t)$, the result of subtracting $V^*_{mean}(t)$, as produced by the PEMD, from $V(t)$. (c) The Hilbert transform of $V'(t)$.

$$\dot{V}=D\nabla^2V-(i_{Na}+i_{K1}+i_{x1}+i_S-i_{ext})/C,$$

$$\dot{y}_k=f(y_k,V), \quad k=2-8, \tag{5}$$

where D is the diffusion coefficient, C is the membrane capacitance, i_{Na} is a fast inward sodium current, i_{K1} is a time-independent outward potassium current, i_{x1} is a time-activated outward current, i_S is a slow inward calcium current, i_{ext} is the external injected current, and y_k are a number of gating variables.

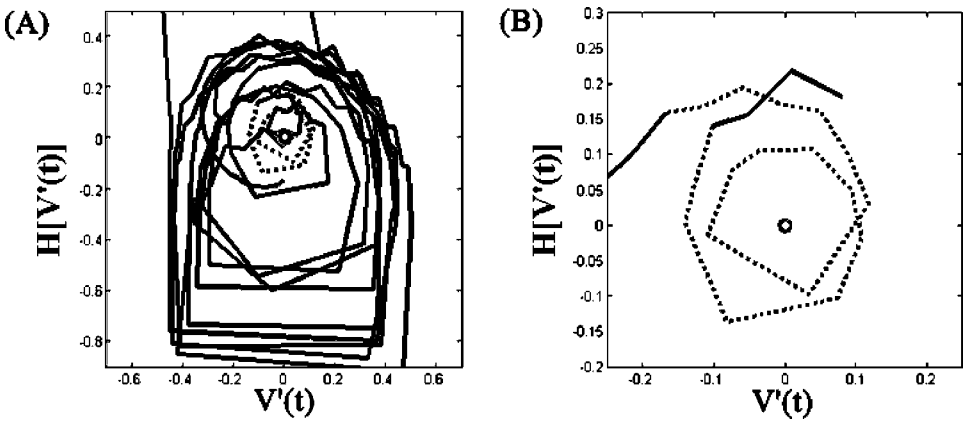

FIG. 4. (a) Example of phase trajectory using Hilbert transform. Circle indicates origin (0,0), same segment from Fig. 1(b) shown as broken line. (b) Expanded view of (a) illustrating the highlighted segment.

The experimental protocols, high-speed optical imaging system, and signal-processing methods have been described previously [11]. A conditioning stimulus (S1) through an electrode renders the tissue in a refractory state. A subsequent premature stimulus delivered through the same electrode (S2), produces unidirectional conduction block such that quatrefoil reentry, a spiral wave pattern with fourfold symmetry, is created. The same stimulation protocol is used for the numerical simulations. For the experimental setup, spatiotemporal movies were recorded at 267 frames/sec in an image format of 96×64 pixels (20.0×13.5 mm) for 300 frames. For the purposes of this manuscript, we express τ in time units (t.u.) of image frames. Spatial and temporal filtering was applied to improve the signal-to-noise ratio. Both the experimental and the numerically simulated data were normalized to the range [0,1] with the resting potential as 0 and the amplitude of the S1 stimulus as 1.

Singularity detection was performed using the algorithm described in [3]. In brief, the concept of topologcal charge is implemented as a series of convolution operations to detect a spatial phase distribution of 2π around a pixel, the distinguishing characteristic of a phase singularity. These points are assigned a topological charge of ±1, depending on chirality; elsewhere, the pixels are assigned a value of zero.

III. RESULTS

The PEMD Hilbert-transformed phase trajectory corresponding to Fig. 1(c) is shown in Fig. 4(a), where it can be seen that each orbit corresponds to a single proper rotation about the origin (0,0). Figure 4(b) is an expanded view of Fig. 4(a), showing a portion of the trajectory with the same segment as in Fig. 1(b) highlighted with a broken line. We see that the origin is encircled by both these loops.

The difference in the phase maps can be seen in Fig. 5. Figure 5(a) shows the phase map using a fixed center of rotation and $\tau=3$, whereas Fig. 5(b) is generated using the PEMD Hilbert-transformed data. Figure 5(c) shows a difference map, the result of subtracting the first two panels from each other. Within the phase map, the phase singularities may be identified as those areas where all the colors converge to a single point. The most significant differences from the time-series method are concentrated around the vicinity of the phase singularities, which is expected since it is those regions where V_{mean} is most likely to miss rotations in the phase plane, while yielding relatively unchanged values at larger distances from the singularities.

The dependence of the localization of the phase singularity on the choice of τ is shown in Fig. 6. Of note is the disparity in the location of the singularities using a constant center of rotation, especially in Fig. 6(c), where extraneous singularities are visible. The singularities created with the PEMD-Hilbert transform bear the most resemblance to those generated using $\tau=3$; while $\tau=7$ was calculated by the autocorrelation function to be the optimal value for the embedded delay, lowering τ to 3 actually provided the least amount of trajectory deformation in the vicinity of the singularities.

We examined the difference between the locations of the singularities as defined using a fixed center of rotation and a τ of 3, and using the PEMD-Hilbert transform. The average difference was 2.3 ± 1.9 spatial units (on a grid of 101×101 units). We also observed that the difference tended to be the greatest when the spiral was experiencing its greatest degree of meander.

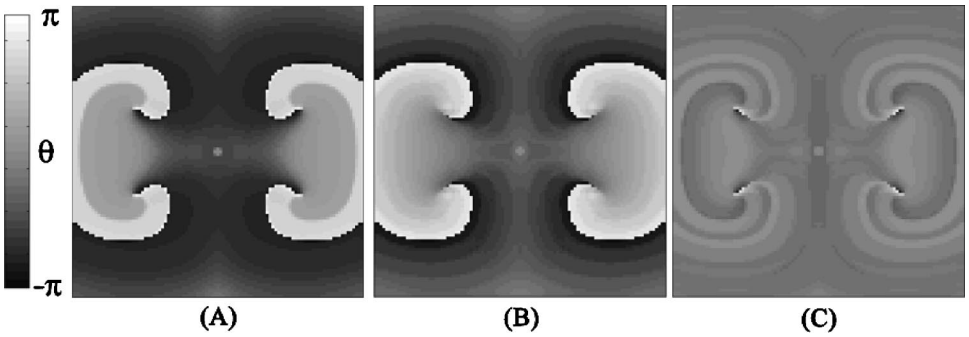

FIG. 5. Comparison of phase maps calculated from numerically simulated data. (a) Map calculated using $\tau=3$. (b) Map calculated using Hilbert transform. (c) Difference map created by subtracting (a) and (b).

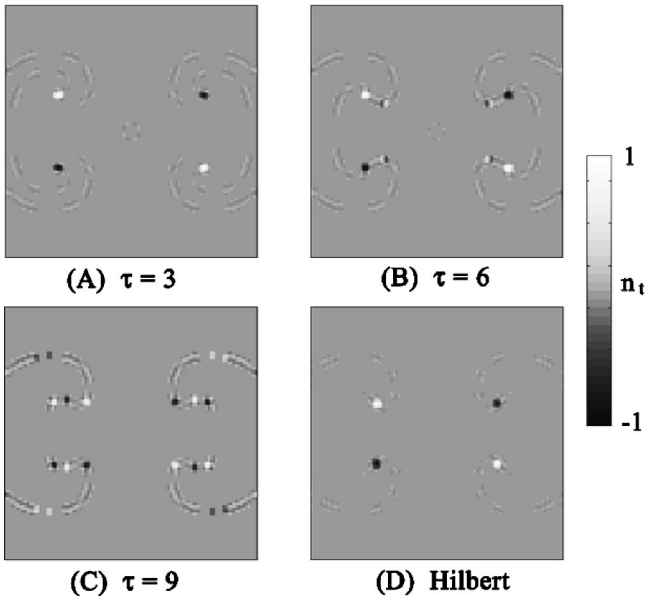

FIG. 6. Comparison of phase singularity maps generated from various values of t and the PEMD-Hilbert transform. (a) $\tau=3$; (b) $\tau=6$; (c) $\tau=9$; and (d) PEMD-Hilbert transform.

Applying this formulation to experimental data [an isochronal activation map is shown in Fig. 7(a)] yields similar results. Figure 7(b) displays an unprocessed sample wave form taken from a data set exhibiting quatrefoil reentry. The dotted regions in Fig. 7(b) highlight a region where a phase singularity is present. The corresponding phase trajectory is shown in Fig. 7(c), which exhibits some improper rotations. Again, we calculate V^*_{mean} for this wave form, generate $V'(t)$, and subsequently $H[V'(t)]$, as seen in Fig. 8. The corresponding PEMD Hilbert-transformed phase trajectory to Fig. 7(a) is shown in Fig. 9(a), where it can be seen that each orbit corresponds to a single proper rotation about the origin (0,0). Figure 9(b) is an expanded view of Fig. 9(a), showing a portion of the trajectory with the same segment as in Fig. 7(a) highlighted with a broken line. Like the numerically simulated wave form, we see that the origin is encircled by these loops.

The difference in the phase maps can be seen in Fig. 10. Fig. 10(a) shows the phase map using a fixed center of rotation and $\tau=7$, whereas Fig. 10(b) is generated using the PEMD Hilbert-transformed data. Figure 10(c) shows the difference map; once again, the regions with the highest difference magnitude are located at the singularities, although some noise can be seen in Fig. 10(b). The average difference in singularity localization between the two methodologies was 0.52 ± 0.47 mm (in a field of view of 20.0×13.5 mm).

An additional consequence of using V^*_{mean} is that we are able to observe the initial phase singularity formation much closer to the start of the S2 stimulus than is permissible with V_{mean}, as shown in Fig. 11. Figure 11(a) is taken at a point 3 t.u. after the beginning of the S2 (S2 terminates after 7 t.u.); the singularities are not visible in the frame generated from V_{mean} because the improper rotations in the phase plane during S2 result in a miscalculation of phase and therefore, a disruption in singularity localization. This finding is important for the purpose of automated phase singularity tracking and for examination of the early dynamics of the phase singularity.

IV. DISCUSSION

Computation of the spatial phase map is important for tracking phase singularity formation and behavior during fibrillatory activity. The standard means of calculating the phase map assumes a constant, fixed center of rotation in the phase plane, which may lead to missed or distorted rotations in the phase trajectory. Detrending the state variable on the basis of oscillation magnitude serves to create a nonstationary origin which takes the temporal evolution of the signal into account. The analytic signal of this state variable generates a proper rotation in the phase plane (a 2π rotation about the origin) while removing the dependence on the choice of time-embedded delay τ. We have observed small differences in singularity localization depending on which methodology is used; while a discussion of absolute localization accuracy is difficult due to the lack of a ''gold standard'' of singularity identification, the PEMD-Hilbert transform algorithm at-

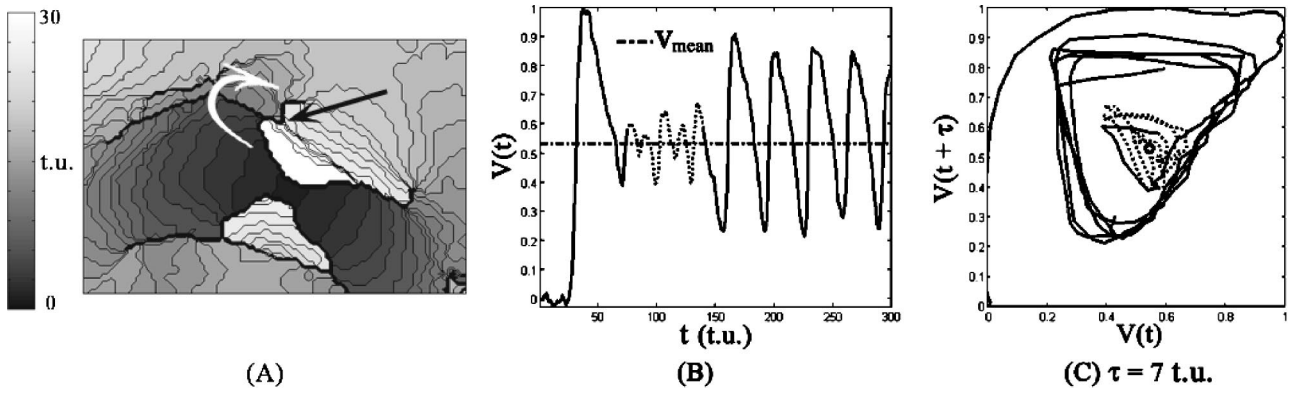

FIG. 7. (a) An isochronal map from experimental data. The white arrow indicates the direction of wave rotation. (b) Transmembrane signal measured at the site indicated by the arrow in (a). Oscillations indicating presence of the phase singularity shown with dotted lines. (c) Phase portrait of the signal shown in (b) using $\tau=7$. Origin (V_{mean},V_{mean}) indicated by circle.

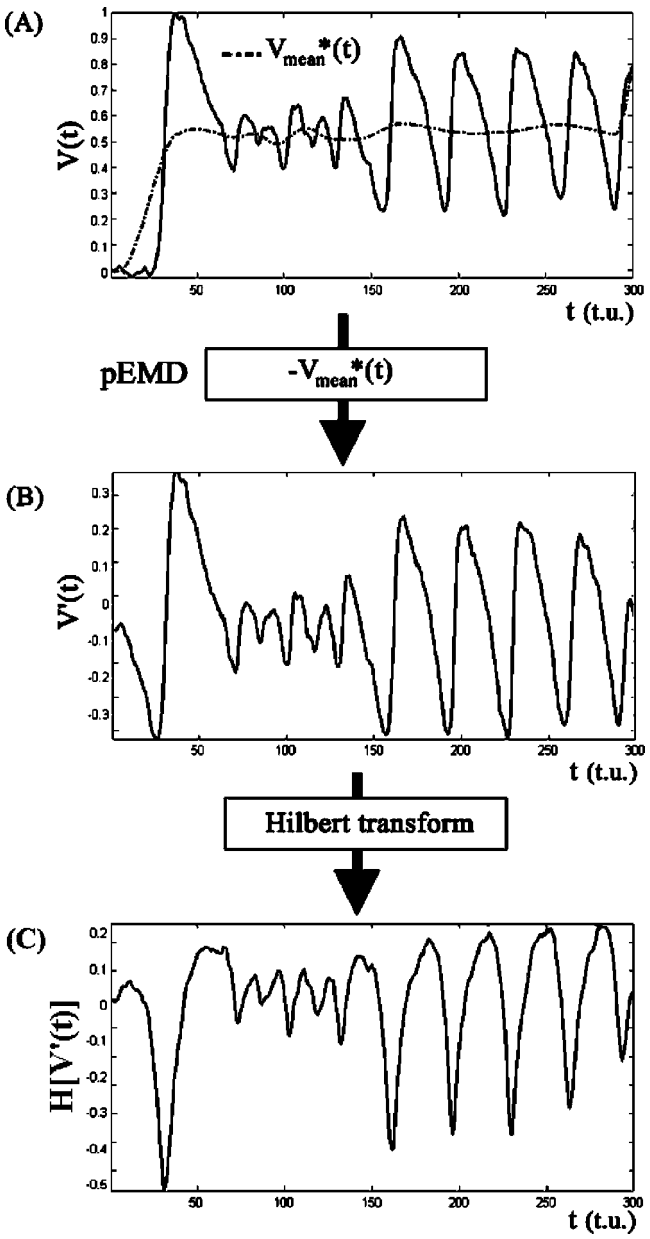

FIG. 8. Flowchart of the algorithm as applied to experimental data. (a) $V(t)$ with $V^*_{mean}(t)$ shown as a broken line. (b) $V'(t)$, the result of subtracting $V^*_{mean}(t)$, as produced by the PEMD, from $V(t)$. (c) The Hilbert transform of $V'(t)$.

tempts to correct for several recognized sources of error. In addition, this method has the effect of enabling phase singularity observation closer to initial formation than previously allowed.

A. Observation of Initial Singularity Formation

Virtual electrodes are critical to phase singularity formation and initial dynamics, and therefore their early detection is important [18,3]. The fact that phase singularities are visible earlier using the PEMD-Hilbert transform algorithm than the constant V_{mean} methodology is evident from Fig. 11; reducing τ to 3 causes the singularities to appear earlier but still not as early as the those produced by the PEMD-Hilbert transform algorithm The question remains as to whether these ''early'' singularities are indeed real or an artifact of the algorithm. In Fig. 12(a), the optical signal during the S2 stimulus from a virtual cathode (V_c) is shown alongside a signal from the virtual anode (V_a). The constant values of V_{mean} for V_c and V_a has been subtracted from both curves such that V_{mean} from this point on is now zero for both curves (shown as a broken line). We see that while the zero-line origin intersects the hyperpolarization trough at V_a, it completely misses the depolarizing peak at V_c. In terms of the phase plane, the depolarization from the virtual cathode advances the phase of this point and initiates reentry by producing an additional cycle (type 0 or even phase resetting) [9]. Hence, the fact that this shift in phase is not captured as a full rotation around the origin in the phase plane is problematic. The appearance of the phase singularity is delayed until a neighborhood of pixels repolarize such that they create a 2π distribution about the origin in the phase plane (recall that singularity detection requires a 2π distribution of phase around a spatial point).

On the other hand, we see that both the anodal and cathodal traces are bisected by $V^*_{a(mean)}$ and $V^*_{c(mean)}$, respectively. Once $V'(t)$ is generated by subtracting these midline traces, both V_c and V_a are distributed about the zero-line origin, as shown in Fig. 12(b). Figure 13 illustrates V_c from Fig. 12(a) in the phase plane created using V_{mean} where the S2 stimulus generates an improper rotation, whereas the use of V^*_{mean} brings the S2 oscillation into a proper rotation. The expected even phase resetting at V_c is clearly seen which, along with V_c, produces an accompanying 2π distribution

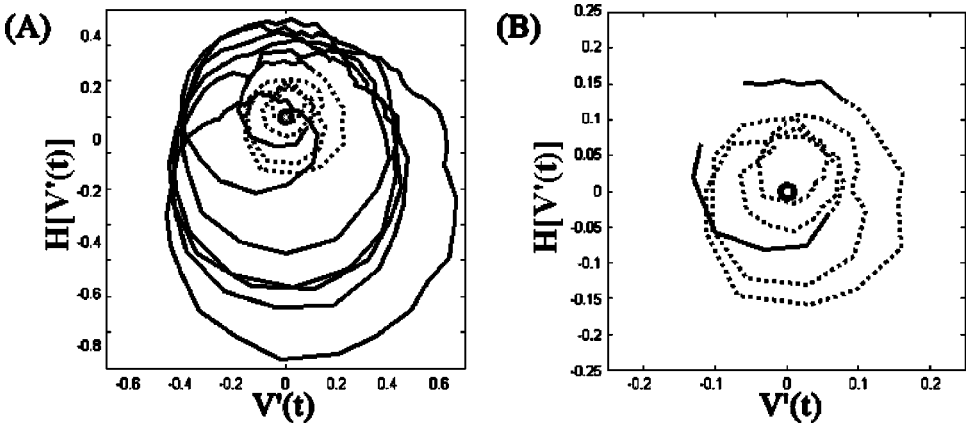

FIG. 9. (a) Example of phase trajectory using PEMD-Hilbert transform. The circle indicates the origin (0,0), the same segment from Fig. 7(b) is shown as a broken line. (b) Expanded view of (a) illustrating the highlighted segment.

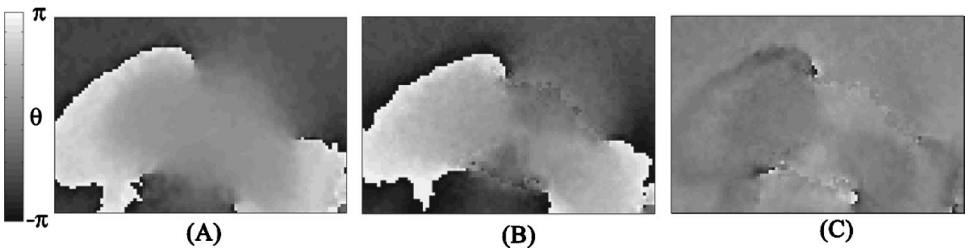

FIG. 10. Comparison of phase maps calculated from the experimental data set used to obtain Figs. 7–9. (a) Map calculated using $\tau=7$. (b) Map calculated using the PEMD-Hilbert transform. (c) Difference map created by subtracting (a) and (b).

of phase around the origin and the appearance of the corresponding singularity at the junction between the virtual electrodes.

B. Limitations

While this method generates proper rotations for selected oscillations in the wave forms, the question still remains of what is the smallest oscillation magnitude which should be allowed a proper rotation. For an example, note the small hump at $t=164$ t.u. in the top panel of Fig. 3 which is missed by V^*_{mean}. The question is whether omitting this peak is acceptable or not. If it is part of a subthreshold response, then it does not matter; unless the phase is reset somewhere in its vicinity, even though the phase value may be calculated differently, a phase singularity will not be detected. If instead it is a low-amplitude response due to its proximity to the reentrant core, shifting its value such that it encircles the origin will cause a phase distortion which may impair singularity localization. In the case of the numerical data of Fig. 3, such a situation causes a slight smearing of the singularity. For experimental data, it is a larger concern since spurious extrema may create unwanted deflections in V^*_{mean}. The magnitude of this issue is dependent on the window size used for the calculation of V^*_{mean}, therefore, a compromise must be made between making the window so short it catches unwanted extrema, or so long that it compromises the selection of the double-peaked potentials. This issue is problematic

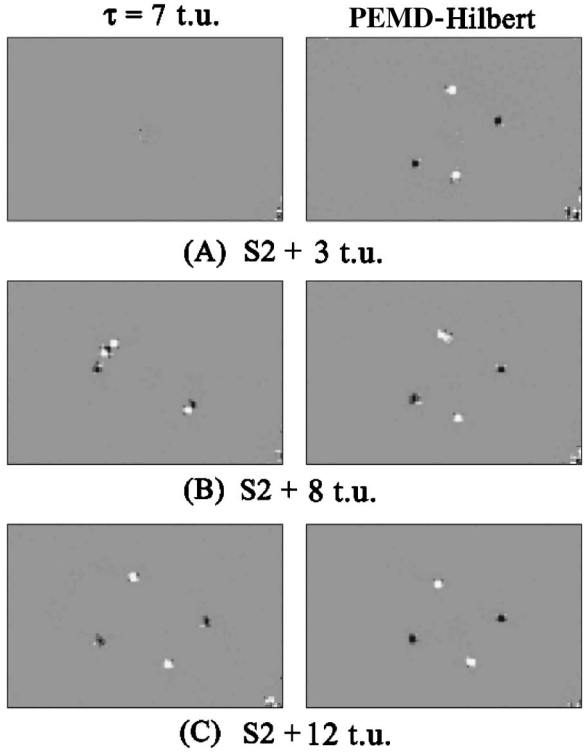

FIG. 11. Phase singularity maps during *S*2 stimulation using experimental data $\tau=7$ (left column) and the PEMD-Hilbert transform (right column). S2 + (a) 3, (b) 8, and (c) 12 t.u.

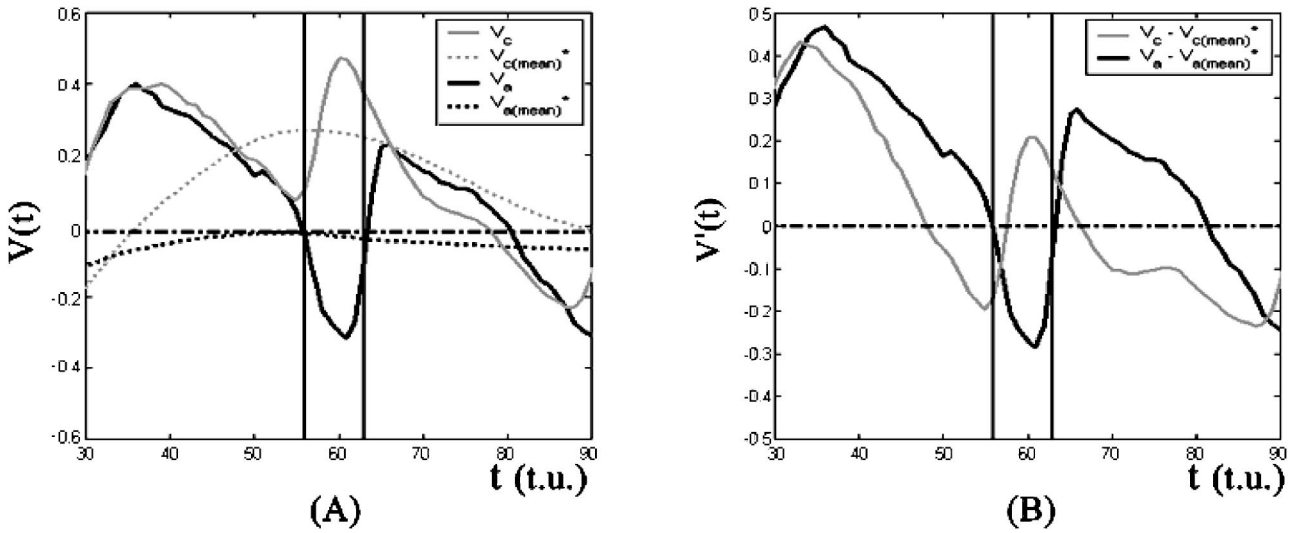

FIG. 12. (a) $V(t)$ traces from point located within virtual cathode (solid gray curve) and virtual anode (solid black curve); corresponding $V^*_{a(mean)}(t)$ and $V^*_{c(mean)}(t)$ traces for each measurement point (dotted lines); V_{mean} defined as zero (broken line). Vertical lines show duration of S2 stimulus. (b) $V'(t)$ traces corresponding to $V(t)$ in (a). Zero line drawn as broken line.

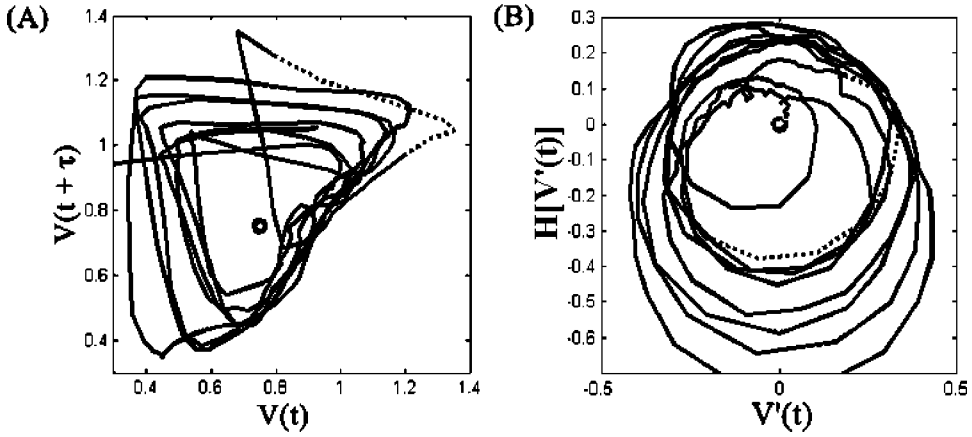

FIG. 13. Phase trajectories for the data at the virtual cathode in Fig. 12 with the segment corresponding to the duration of S2 stimulus shown as dotted line. (a) $\tau=7$, (b) PEMD-Hilbert transform.

because an excursion in V^*_{mean} is not transient but instead occurs over a duration lasting the length of time from the previous extrema to the subsequent extrema. Hence, phase values can be distorted over a wide length of time.

As mentioned above, it is worth noting that a small value of τ produces results similar to the PEMD-Hilbert algorithm, as compared to the larger value determined by the autocorrelation function (Fig. 7). For the time-delay embedding method, choosing a value of τ close to the duration of the action potential upstroke tends to minimize the trajectory distortion in the phase portrait, especially in the case of fibrillation where the upstroke duration is prolonged [2]. Therefore, globally choosing a short τ for the time-delay embedding method achieves the same desired effect in the phase plane as the orthogonality of the Hilbert-transformed signal.

The algorithm presented still possesses a time-dependent component, the calculation of the PEMD; the effectiveness of the Hilbert transform is dependent on the proper determination of the PEMD. The window length is currently chosen not on the basis of the double oscillations themselves but inferred on the basis of the full action potentials. Using half the period of the full potential seems to be successful in most cases tested but this assumption may not apply to every set of cardiac wave forms. Setting the filter window too large may cause small oscillations situated between larger ones to be omitted entirely; setting the window too small runs the risk of incorrectly capturing deflections due to noise. Based on our experience, we have found it more desirable to err on the side of a shorter window when selecting the optimal window length. A more rigorous criterion for calculating the PEMD is a subject for future research.

ACKNOWLEDGMENTS

This study was supported in part by NIH Grant Nos. P01HL46681, R01HL58241, and T32HL07411 and a Biomedical Engineering Research grant from the Whitaker Foundation. We thank Richard Gray for his comments and suggestions.

[1] R.A. Gray, A.M. Pertsov, and J. Jalife, Nature (London) **392**, 75 (1998).
[2] R. A. Gray and J. Jalife, in *Cardiac Electrophysiology: From Cell to Bedside*, 3rd ed., edited by D. P. Zipes and J. Jalife (Saunders, Philadelphia, 1999), p. 432.
[3] M.-A. Bray *et al.*, J. Cardiovasc. Electrophysiol. **12**, 716 (2001).
[4] Chen, *et al.*, Circ. Res. **86**, 86 (2000); Chen, *et al.*, Curr. Sci. **48**, 220 (2000); Samie, *et al.*, Circ. Res. **89**, 1216 (2001).
[5] R. FitzHugh, Phys. Rev. Lett. **1**, 445 (1961).
[6] N.H. Packard, J.P. Crutchfield, J.D. Farmer, and R.S. Shaw, Phys. Rev. Lett. **45**, 712 (1980).
[7] F. Takens, in *Dynamical Systems and Turbulence*, edited by D. A. Rand and L.-S. Young. (Springer-Verlag, Berlin, 1980), p. 366.
[8] H.D.I. Abarbanel, R. Brown, J.J. Sidorwich, and L.S. Tsimring, Rev. Mod. Phys. **65**, 1331 (1993).
[9] A. T. Winfree, *When Time Breaks Down: The Three-Dimensional Dynamics of Electrochemical Waves and Cardiac Arrhythmias* (Princeton University Press, Princeton, NJ, 1987).
[10] A.M. Pertsov *et al.*, Circ. Res. **72**, 631 (1993).
[11] S.-F. Lin, B.J. Roth, and J.P. Wikswo, Jr., J. Cardiovasc. Electrophysiol. **10**, 574 (1999).
[12] T. Yalcinkaya and Y.-C. Lai, Phys. Rev. Lett. **79**, 3885 (1997).
[13] N.E. Huang *et al.*, Proc. R. Soc. London, Ser. A **454**, 903 (1998).
[14] M.A. Allessie, F.I.M. Bonke, and F.J.G. Schopman, Circ. Res. **23**, 54 (1973).
[15] B. Olshansky, D. Moreira, and A.L. Waldo, Circulation **87**, 373 (1993).
[16] D. Gabor, J. Inst. Electr. Eng. (London) **93**, 429 (1946).
[17] B.J. Roth, J. Cardiovasc. Electrophysiol. **8**, 768 (1997).
[18] J.P. Wikswo, Jr., S.-F. Lin, and R.A. Abbas, Biophys. J. **69**, 2195 (1995).